Snow stratigraphy observations from Operation IceBridge surveys in Alaska using S/C band airborne ultra-wideband FMCW radar

Jilu Li, Fernando Rodriguez-Morales, Carl Leuschen, John Paden, Daniel Gomez-Garcia, Emily Arnold

The Center for Remote Sensing of Ice Sheets, University of Kansas, Lawrence, KS 66045, USA

5   *Correspondence to*: Jilu Li (jiluli@ku.edu.com)

Abstract. During the concluding phase of the NASA Operation IceBridge (OIB), we successfully completed two airborne measurement campaigns (in 2018 and 2021, respectively) using a compact S/C band radar installed on a Single Otter aircraft and collected data over Alaskan mountains, ice fields, and glaciers. We observed snow strata in ice facies, wet-snow/percolation facies and dry snow facies from radar data. This paper reports seasonal snow depths derived from our

10   observations. We found large variations in seasonal radar-inferred depths assuming a constant relative permittivity for snow equal to 1.89. The majority of the seasonal depths observed in 2018 were between 3.2 m and 4.2 m, and around 3 m in 2021. We also identified the transition areas from wet-snow facies to ice facies for multiple glaciers based on the snow strata and radar backscattering characteristics. Our analysis focuses on the measured strata of multiple years at the caldera of Mount Wrangell to estimate the local snow accumulation rate. We developed a method for using our radar readings of multi-year

15   strata to constrain the uncertain parameters of interpretation models with the assumption that most of the snow layers detected by the radar at the caldera are annual accumulation layers. At a 2004 ice core and 2005 temperature sensor tower site, the locally estimated average snow accumulation rate is ~2.89 m w. e. a-1 between the years 2002 and 2021. Our estimate of the snow accumulation rate between 2005 and 2006 is 2.82 m w. e. a-1, which matches closely to the 2.75 m w. e. a-1 inferred from independent ground-truth measurements made the same year. We also found a linear increasing trend of 0.011 m w. e.

20   a-1 per year between the years 2002 and 2021. With this trend, we extrapolated the snow accumulation back to 1992 and obtained an average accumulation rate of 2.74 w. e. a-1 between the years 1992 and 2004, which agrees well with the value of 2.66 w. e. a-1 for the same period determined from the ice core data retrieved at the caldera in 2004. The results reported here verified the efficacy of our method, its assumption, and the interpretation models.

1 Introduction

25   Glaciers outside Greenland and Antarctica play an important role in the Earth's ecosystem. They respond to climate dynamics in a unique way, potentially contributing to global sea level and having an impact on regional hydrology and economy. According to a recent report [WCRP Global Sea Level Budget Group, 2018], these glaciers are the second largest contributor to sea-level rise, after ocean thermal expansion, contributing 21 percent of the global mean sea-level rise during the period between 1993 and 2018. Another study claims that global glaciers are increasingly losing ice mass since the twenty first

30 century, contributing 6 to 19 percent of the observed acceleration of sea-level rise during 2000-2019, and the mass loss of Alaska glaciers is the biggest contributor, accounting for 25 percent of the global glacier mass loss compared to the second largest contributor, glaciers of the Greenland periphery, with 13 percent [Hugonnet et al., 2021]. The volume loss of the glaciers in Alaska is ~10 percent of the estimated total mean annual freshwater discharged into the Gulf of Alaska (Neal et al., 2010 and Hill et al., 2015), and the glacier discharges affect stream flow and stream temperature that are critical to the spawning

35 and incubation of Pacific Salmon in the Copper River region of the Gulf of Alaska, which is home of important fisheries [Shanley and Albert, 2014].

Snow depth and accumulation on glaciers are key components to understand and model the process of glacier mass loss. Existing satellite-borne remote sensing techniques are routinely used to map snow cover extent. However these observations

40 offer limited capabilities for deriving snow depth and snow water equivalent (SWE). For active microwave sensors, only wet snow can be recognized reliably. However high water content severely reduces the signal penetration depth into the snow. Passive microwave sensors can map dry snow, but their spatial resolution is coarse and only ~1 m snow depth can be mapped [Dietz et al., 2012]. For ground-based measurements, snow depth and accumulation are usually estimated using *in-situ* probe and /or snow pit measurements [Benson, 1968; Kanamori et al., 2005; Stuefer et al., 2020], automatic records from snow

45 pillow, temperature sensors and weather stations [Beaumont, 1965; Kanamori et al., 2008], and measurements from ground-penetrating radar (GPR) [McGrath et al., 2015]. Ground-based methods provide detailed measurements about snow properties including temperature, snow grain shape and size, hardness, density, and layer information. The major drawback of ground-based methods is that they are either sparse point observations or only provide very limited continuous spatial coverage. Airborne remote sensing with GPR and FMCW (Frequency-Modulated Continuous Wave) radar has been demonstrated to be

50 a cost effective method to provide measurements with fine spatial resolutions and comprehensive regional coverage [McGrath et al., 2015; Yan et al., 2017]. Ground-based measurements are used to validate both airborne and satellite observations and airborne data can also be used to validate satellite observations [Lindsay, et al., 2015; Ramage, et al., 2017; Largeron, et al., 2020; Jeoung et al., 2022].

55 Direct snow depth and layer measurements at glacier-scale are rare in Alaska because of their difficult accessibility. Arcone [2002] analyzed data collected in the early summer of 1994 by a helicopter-borne 135 MHz short-pulse radar over the Bagley Ice Field and provided estimates of snow depths and refractive indices based on diffraction and reflection characteristics of snow layers of temperate firn. In the spring of 2013, Gusmeroli et al. [2014] and McGrath et al. [2015] measured snow accumulation of several glaciers around the Gulf of Alaska using 500 MHz ground- and helicopter-based ground-penetrating

60 radar instruments. Complemented by ground truth observations, they showed highly variable SWE over short spatial scales. In the late spring of 2018, Li et al. [2019] collected snow data over Alaskan glaciers, ice fields and mountain caps using a compact ultra-wideband FMCW radar installed on a Single Otter aircraft. The radar operated at a center frequency of 5GHz with 6-GHz bandwidth. They observed seasonal snow depth around the areas of Logan Glacier, Walsh Glacier and upper

Hubbard Glacier, as well as deep multiyear snow stratigraphy of the snow caps of Wrangell and Bona mountains. For the snow

65   cap of Mount Wrangell, Benson [1968] obtained detailed profiles of the temperature, density, hardness, stratigraphy, snow depth and accumulation using the snow pit measurements to the depth of 10 meters taken during the summer of 1961. A more recent study determined the snow accumulation at the summit of Mount Wrangell according to the burial times of temperature sensors during the accumulation period between the June 2005 and June 2006 [Kanamori et al., 2008].

70   In the spring of 2021, we had a follow-up airborne campaign in Alaska at the closing of the NASA OIB and observed snow stratigraphic layers in much broader coverage than the 2018 campaign. The objective of this paper is to report our new snow depth observations, derive preliminary SWE values and snow accumulation with the combined 2018 and 2021 airborne radar datasets, and compare the results with previous observations and studies. The paper is organized as follows: Section 1 is the introduction and provides the background information of the study; Section 2 describes the data collection and processing

75   activities; Section 3 presents radar observational results, analysis methods and discussions; and Section 4 summarizes the significant findings and draws conclusions.

2 Data collection and processing

We conducted the 2021 OIB Alaska campaign between May 2, 2021 and May 13, 2021. During this period, we collected ~2 TB of snow radar data over a span of 8 days, covering ~5315 linear km. The campaign base (Ultima Thule Lodge), the aircraft

80   platform (Single Otter), antenna installation, and on-board LiDAR and radar are largely the same as in the 2018 campaign [Li, et al., 2018]. In order to be adaptive to the large variations in the altitude above the ground (AGL) during the flight caused by the complex mountain topography, we operated our snow radar with a 4-GHz bandwidth between 2 GHz and 6 GHz instead of 2-8 GHz as done in 2018. This restricts the de-ramped received signals to the first Nyquist zone (<62 MHz), thereby setting the maximum survey altitude to ~586 m (~1923 ft.) AGL. The bandwidth reduction results in a commensurate degradation in

85   vertical resolution, but this would not affect the signal-to-noise ratio and snow penetration in a significant manner. Rodríguez-Morales et al. [2021] and Li et al. [2019] give the details about the compact snow radar development, key system parameters and the general instrument configuration used onboard the Single Otter aircraft. Additionally, more recent changes and improvements made to the system are documented in Rodriguez-Morales et al. [2021].

90   Figure 1 shows the flight lines of the 2021 campaign (brown and blue) together with the lines flown in 2018 (green and red) with the locations of Ultima Thule Lodge, Mount Wrangell, Mount Bona, the Bagley Ice Field and a few glaciers annotated on the hillshade map. The latitudes and longitudes of these flight lines are within [59.6151°N 63.7411°N] and [138.5295°W 147.9042°W] respectively. The major part of the areas surveyed during the two campaigns overlap with each other. The spatial sampling for a few glaciers (Nabesna Glacier, for example), the Bagley Ice Field and the snow cap of Mount Wrangell is

95   denser in 2021 as compared to the flight lines in 2018. This was achieved by using zig-zag and gridded flight lines. The new

areas surveyed in 2021 include Yahtse Glacier and Malaspina Glacier on the coast of Alaska Gulf; Columbus Glacier and Seward Glacier on the east of Bagley Ice Field; and Kaskawulsh Glacier in Canada's Kluane National Park and Reserve.

After the campaign, we first compared the elevation measurements over flat and smooth surfaces with the simultaneous laser measurements and calibrated the radar system delay. We processed the radar data with differential GPS and INS information to improve the geolocation accuracy. The main data processing steps included removal of coherent noise, phase correction and time shift to correct for aircraft altitude variation, Fourier transformation to obtain target response as a function of range, coherent and incoherent integrations to improve signal-to-noise ratios and fading effects, and deconvolution to reduce range sidelobes [Panzer et al. 2013; Yan et al., 2017]. Unlike the campaigns in Antarctica and Greenland, where open water leads were occasionally available as specular targets for deriving the radar's system impulse response and then using these data for deconvolution, during the two Alaska campaigns, we used data collected over the water surface of lakes by the coast for deconvolution. Supplementary section S1 presents the radar's system impulse response derived using the reflections from the surface of Malaspina Lake during the 2021 campaign, and sample radar echograms and A-scopes showing the range sidelobe reduction obtained by means of our deconvolution algorithm.

3 Result analysis and discussions

We observed snow layers of seasonal accumulation and multi-year accumulation over a range of surface elevations from 1007 m to 4621 m above the sea level. These observations were from ablation areas at lower elevations all the way up to mountain summits at high elevations. In this section, we first present the overall seasonal snow observations, then focus on analyzing snow accumulations at the caldera of Mount Wrangell, and lastly discuss the observations of the transition from accumulation to ablation along several glaciers.

3.1 Observations of seasonal snow

The red and blue flight lines in Fig. 1 show the locations where we picked the seasonal snow layer in both 2018 and 2021, respectively. This layer may be the earlier old ice in ablation areas or the first distinct layer in accumulation areas. The first distinct layer in accumulation areas may have ambiguity to be the previous summer layer when snow layers exist within the annual layer for deep snow cover. Figure 2(a) presents a radar echogram for a 10-km segment along the main trunk of the east Bagley Ice Field. The red line in the map of Fig. 2(b) shows the geolocation where we retrieved the radar data on May 2, 2021. The glacier surface profile is flattened in Fig. 2(c) to better show the snow depth, which is around 3 m. The surface elevation of this segment is between 1326 m and 1423 m in the ablation area (see Table 3 and Fig. S4-5). Figure 2(d) and (e) give the distributions of tracked seasonal snow depth for both 2018 and 2021, respectively. For the 2018 data, the snow depths are generally between 3.2 m and 4.2 m. For the 2021 data, the snow depths are around 3 m. There is a second distribution peak around depth of 1 m for both 2018 and 2021 datasets. Given the low number of occurrences, we truncated both distributions for depths beyond 8 m. It is noted that there are few locations at high elevations where the seasonal snow depth could be greater

4

than 15 m. For the snow depth calculations, we used a value of 1.89 for the real part of the relative permittivity. This value is from the mean velocity of CMP (common midpoint) and probe measurements at seven glaciers in Alaska, 2.18×10^8 m/s

130   [McGrath et al., 2015]. We note that the Bagley Ice Field is a temperate glacier, and previous investigations based on 135-MHz pulsed radar measurements in early summer 1994 determined refractive indices from 4.1 to 4.5 for the near-surface of Bagley Ice Field. This range of indices corresponds to much higher values of the relative permittivity than 1.89 because the 1994 measurements were taken in the early summer when significant melting and drainage occurred [Arcone, 2002].

3.2 Observations over mountain summits

135   Snow covers with clear annual layers at high-latitude-and-high-elevation mountain summit areas contain information about the past climate of the area. Several ice cores were drilled decades ago at the caldera of Mount Wrangell and at the Mount Bona-Churchill saddle to study the local climate history [Benson, 1984; Holdsworth et al., 1992; Goto-Azuma et al., 2003; Fisher et al., 2004; Shiraiwa et al., 2004; Zagorodnov et al., 2005; Yalcin et al., 2006; Urmann 2009]. Mount Wrangell (62°00'21" N, 144°01'10" W, 4317 m a.s.l.) is a massive active shield volcano with an ice-filled caldera extending 4 by 6 km

140   in diameter at its broad summit. The summit region above 4000 m. a.s.l. is over 3 by 8 km and extends into dry snow zones. Because of these features, it drew the attentions of researchers to study the glacier-volcano interaction [Benson et al., 1975; Benson et al., 2007; Garry et al., 1989], and ice core and climate records [Benson, 1968; Benson, 1984; Yasunari, et al., 2007; Kanamori et al., 2008; Matoba et al., 2014]. Mount Bona (61°23'08" N, 141°44'55" W, 5040 m a.s.l.) and Mount Churchill (61°25'10" N, 141°42'53" W, 4766 m a.s.l.) are both ice-covered stratovolcanoes. Mount Bona is about 3 km to the southwest

145   of Mount Churchill, and the saddle area between them are 4.2 km by 2.7 km elliptical. The Bona Churchill Ice Core BC1 (460.96 m), drilled to bedrock at the saddle (61°24' N,141°42' W, 4420 m a.s.l.) in the spring of 2002, is one of the only annually dateable records of extended historical duration to ever be recovered from the northeastern side of the Pacific Basin [Urmann 2009]. A recent study of stable oxygen isotopes (δ18O) in the ice core revealed a strong connection between isotopes at the BC1 site and western Arctic climate [Porter et al., 2019].

150

To map the annual snow layers formed in recent years around these two areas, we flew over the Mount Wrangell summit on May 25, 2018, May 3, 2021 and May 9, 2021, respectively; and over the Bona-Churchill saddle along southeast-northwest and southwest-northeast flight lines on May 30, 2018 and May 9, 2021, respectively. Figure 3 shows the data coverage of the above surveys. In this figure, the dots with visible spacing depict the flight lines and the dots without visible spacing mark the

155   locations where subsurface layer were observed; the red and blue dots represent the flight lines of 2018 and 2021 respectively. As shown by the red dots in Fig. 3(a), it was only a single path through the caldera center of Mount Wrangell in 2018. The path was from east to west and then repeated from the west to east. In 2021, in addition to repeating the flight path of 2018, we surveyed the whole caldera in grids of 1-km spacing along west-east and north-south flight lines. In Fig. 3(a), the black triangle marks the summit of Mount Wrangell. The red star marks the approximate location of the snow accumulation

160   measurements made in 2005 by using temperature sensors installed on a tower at (61°59'26.88" N, 144°01'32.16" W, 4070.41

m a.s.l.), which is also the 2004 ice core drilling site [Kanamori et al., 2008]. The green star marks the location of the crossover between the 2018 and 2021 flight lines at (61°59'09.24" N, 144°00'24.48" W, 4040.32 m a.s.l.). The two locations marked by the stars correspond to the study sites discussed in this section. As shown in Fig. 3(b), the flight lines cross the Bona-Churchill saddle roughly orthogonally along the southwest-northeast and northwest-southeast directions, respectively. The black and red

165 triangles mark the summit locations of Mount Bona and Mount Churchill, respectively. The red star marks the BC1 ice core site drilled at the saddle in 2002. The green star annotates the location of the data collection segment used to produce the sample radar echogram given in Fig. 4(d). Figure 4(a) is a radar echogram obtained from data collected by flying from north to south over the summit of the Mount Wrangell and the site of the 2004 ice core and 2005 temperature sensor measurements at the caldera center. Figure 4(b) is plot of the flight line (in red) on a map with the ice core location annotated by a blue circle.

170 Figure 4(c) displays the conformable sub-surface strata across the caldera. Figure 4(d) presents a radar echogram produced from data collected by flying over the Bona-Churchill saddle, showing the dense accumulation layers near the BC1 ice core site. In Fig. 4(c) and (d), the surface profiles are again flattened to display the snow layers; the deepest snow depths observed are ~ 81 m at the 2004 ice core site in the caldera of Mount Wrangell and ~ 50 m near the BC1 ice core site at the Bona-Churchill saddle. At a different location marked by the green circle on the map in Fig. 3(b), the deepest layer observed is ~128

175 m (see the radar echogram provided in the supplementary section S2). For the depth calculation here, we assume an effective relative snow permittivity of 2.96 obtained according to the interpretation and empirical snow density-permittivity models at the 2004 ice core site in the caldera of Mount Wrangell as described below.

Because there is no snow pit and ice core data available at the time of the radar measurements, we adopt the following
180 interpretation models [Garry et al., 1989] to estimate the approximate depositional ages of the observed snow layers and the averaged water equivalent accumulation rate over these depositional ages:

$$\frac{dp}{dz} = \rho g cos\alpha \tag{1}$$

$$\frac{d\rho}{dz} = \begin{cases} m_1\rho^2(\rho_I - \rho/\rho_I) & p \le p^* \\ m_2\rho^2(\rho_I - \rho/\rho_I) & p > p^* \end{cases} \tag{2}$$

$$\frac{dw}{dz} = -\frac{w}{\rho}\frac{d\rho}{dz} - \Delta \tag{3}$$

185 $$\Delta(z) = \begin{cases} \Delta_0 & z \le z_s \\ 0 & z > z_s \end{cases} \tag{4}$$

$$\frac{dt_a}{dz} = \frac{1}{w} \tag{5}$$

$$\frac{dt_z}{dz} = \frac{2\sqrt{\varepsilon}}{c} \tag{6}$$

$$\varepsilon = (1 + 8.5 \times 10^{-4}\rho)^2 \tag{7}$$

190 The differential Equations (1)-(3), (5) and (6) respectively describe the variations of pressure p, density ρ, downward velocity w, depositional age t_a, and two-way travel time (TWTT) from the surface to the depth t_z, respectively with depth z. In Eq.

6

(1), $g = 9.80 \ m/s^2$ is the gravitational acceleration, and α is surface slope. Equation (2) is a modified version of Benson's model [Benson, 1996] in the form of critical pressure p^* with $m_1 = 16.0 \times 10^{-5} \ m^2/kg$, $m_2 = 4.3 \times 10^{-5} \ m^2/kg$, $p^* = 4.459 \times 10^4 \ Pa$, $\rho(0) = \rho_s = 377.36 \ kg/m^3$, the initial snow density at the surface, and $\rho_I = 917.4 \ kg/m^3$, the ice density; these empirical constants were determined from Greenland measurement but fit well to the Mount Wrangell measurements of firn density [Garry et al., 1989]. In Eq. (3), the initial condition is $w(0) = w_s = \rho_w b_w / \rho_s$, where w_s is the annually averaged volume flux of snow at the surface, ρ_w the water density, and b_w the annual water equivalent accumulation at the surface; the flow divergence Δ is assumed to be constant as Δ_0 to the stagnation depth z_s and to be zero at greater depths as described by Eq. (4) with $z_s = 150 \ m$. Equation (6) describes the two-way travel time t_z of the electromagnetic wave through the snowpack, where $c = 2.9979 \times 10^8$ m/s is the velocity of light in free space. Equation (7) describes an empirical law for the effect of firn density on relative permittivity [Robin et al., 1969], where ρ is measured in kg/m^3. Equation (7) is similar to Eq. (1) in [Tiuri et al., 1984], which was verified by laboratory dry snow measurements made at four frequencies at 850 MHz, 1.9GHz, 5.6GHz and 12.6 GHz.

Steady-state conditions are implied by the coupled equations above. The central region of the summit caldera of Mount Wrangell were thought to be near steady-state [Benson and Motyka, 1978] based on repeated surveys showing that the surface elevation remained constant within 1 m from 1965 to 1978 [Bingham, 1967; Motyka, 1983]. By looking at the crossovers of the repeated paths flown in 2018 and 2021, the surface elevations are close to zero at elevations ~4100 meters (See supplementary section S3 for details). Therefore the net surface accumulation is roughly balanced by basal melting and outflow to Long Glacier, and we conclude that the steady-state conditions still hold at the time we took measurements.

With given initial conditions, we simultaneously integrate the coupled equations to solve for the depositional ages of the observed snow layers. In the previous study by Garry et al., 1989, $b_w = 1.3 \ m/yr$ and $\Delta_0 = 6.075 \times 10^{-3}/yr$ were used based on surface accumulation and motion measurements made in 1965 [Benson et al. 1975], 1965-1966 [Bingham, 1967], and 1975-1976 [Motyka, 1983]. To consider the surface condition changes since then and the spatial variations, we study the sensitivities of the solved depositional ages to these two parameters, and determine their appropriate values using the TWTT of snow layers measured by radar as the constraints (other initial conditions and parameters are the same as used by Garry et al., 1989). This is done by minimizing the following cost function:

$$J = \sqrt{\sum_{i=1}^{N}[(t_{a_{i+1}} - t_{a_i}) - 1]^2} \tag{8}$$

where N is the number of observed layers including the surface with index $i = 1$ and $t_{a_1} = 0$. We thus come up with this cost function by assuming that most observed snow layers are annual accumulation layers and the difference between any two consecutive layers should be close to 1.

225

We choose a location where the surface slope is zero to illustrate our method. Figure 5(a) and (b) show the 2018 and 2021 radar echograms with the surface tracked by a red line and snow layers tracked by blue lines (the depth axis is plotted with effective relative snow permittivity of 2.89 and 2.96, respectively, estimated from the interpretation models respectively). The red dashed lines in each echogram mark the crossover of the flight lines and the location is ~1.127 km to the 2004 ice core site

230   and the snowfall measurements using temperature sensors [Kanamori et al., 2008]. Figure 5(c) and (d) presents, respectively, the A-scopes at the crossover point and the picked layer images of only 50 data lines after the crossover point. The horizontal red lines annotate the TWTT measured by the radar at each picked layer. We performed along-track filtering to display the layers more clearly in Fig. 5(c) and (d) and enumerated the picked layers using numbers with number 1 representing the surface. These annotation numbers are the layer indices in Equation (8) and Table 1. For the given initial conditions and model

235   parameters, we first solve Equations (1)-(7) by integration from the surface to the depth of 100 m to determine the relationship between layer depositional age and TWTT. The blue lines in Fig. 5(e) and (f) show the model result from the 2018 and 2021data frames, respectively. The depositional ages of the observed snow layers are then determined according to the TWTT from the surface to each layer measured by the radar as shown by the red circles on the top of the blue lines in Fig. 5(e) and (f). The cost function J is computed according to Eq. (8) for a range of b_w. For the 2018 data frame, there are 16 layers observed and

240   b_w is increased from 1.3 m/yr to 5.2 m/yr in steps of 0.1 m/yr. For $\Delta_0 = 7.3 \times 10^{-3}/yr$, the variations of the cost function with b_w is shown by the blue line in Fig. 6(a). Because the empirical $\varepsilon \sim \rho$ law determines the model-based travel velocity of the radar signals in snowpack, and thus the modelled $t_a \sim t_z$ relationship, we also computed the cost function using the following empirical equation [looyenga, 1965]:

245    $$\varepsilon = [\frac{\rho}{\rho_I}(\varepsilon_I^{1/3} - 1) + 1]^3 \qquad\qquad (9)$$

where $\varepsilon_I = 3.17$ is the relative permittivity of ice. As shown in Fig. 6(b), the relative permittivity difference between the two empirical laws described by Eq. (7) and Eq. (9) is less than 3% from the surface to the depth of 100 m, and the effect of this difference on the cost function (as shown in Fig. 6(a)) can be ignored. Therefore, all the subsequent analyses here will only

250   consider the results using Eq. (7). According to Fig. 6(a), the best estimate of b_w is $\sim 3.3\ m/yr$. Figure 7 shows the variations of the cost function versus Δ_0 over a range between 0.25 to 2 times of $6.075 \times 10^{-3}/yr$. We can see the vales of the cost function do not change much, and the best estimate of Δ_0 is $7.3 \times 10^{-3}\ /yr$, or 1.2 times $6.075 \times 10^{-3}/yr$. Similarly, we determined the optimal values of b_w and Δ_0 for the 2021 data at the crossover, which turned out to be $3.3\ m/yr$ and $7.6 \times 10^{-3}\ /yr$; and for the 2004 ice core and 2005 temperature sensor tower site, which turned out to be 3.0 m/yr and $3.9 \times 10^{-3}\ /yr$.

255

Table 1 lists the estimated depositional ages of the 16 tracked layers in the 2018 data frame and 19 tracked layers in the 2021 data frame at the crossover point (with the cost function $J = 1.11\ and\ 1.08$ years respectively), and 21 layers on the 2021

data frame at the 2004 ice core and 2005 temperature sensor tower site (with the cost function $J = 1.33$ years). From this

table, we see that most of the layers at the crossover area are identified as annual layers. The 4th, and 11th layers in the 2018

260   echogram are identified as the accumulation layers between annual layers based on their estimated depositional ages; similarly,

the 7th and 14th layers in the 2021 echogram are accumulation layers between annual layers. The repeated radar measurements

at the same spot after three years enable us to observe how the snow accumulation layers move downwards. However, there

exist some shifts in the estimation of depositional ages of the snow layers between the crossover and the ice core/tower site.

The shift increases to ~2 years at the 20th layer. The estimation shifts between different sites are expected, considering the

265   snow accumulation process is very complex and are highly affected by the interplay between complex topography and wind

redistribution [Winstral et al., 2002]. The surface of the ice core/tower site has a grade of ~2° while the crossover is at a local

valley and the effect of wind redistribution on the snow accumulation is not included in the interpretation models.

Our purpose in this study is not to estimate the accurate depositional age of each snow layer but rather the average snow

270   accumulation rate over years. The annual accumulation rate $r_a(k)$ is estimated according to

$$r_a(k) = \sum_{z_{k-1}}^{z_k} \frac{\rho(z)}{\rho_w} \, dz \qquad (10)$$

where k is the depositional age in integer year and $\rho(z)$ is the model-derived density-depth function. The effects of wind

275   redistribution and other factors resulted in the differences in the TWTT measured by the radar for the same snow layers at

different locations and thus the depositional age estimate. These effects have been partly compensated by the optimal values

of b_w and Δ_0, and will be further reduced when we estimate the average accumulation rate over multiple years.

Figure 8 presents the annual accumulation rates estimated at the two study sites from the interpretation models with the

280   parameters b_w and Δ_0 constrained by the TWTTs to accumulation layers measured by radar. The blue, green, and red circles

in the figure present the annual snow accumulation rate estimates, respectively, at the crossover from the 2018 and 2021 radar

frames and at the ice core/tower site from 2021 data frame. The blue and red solid lines are the linear fitting of the estimates

at the crossover and the ice core/tower site, respectively, and the blue and red dashed lines are extrapolations to the year 1992.

The interpretation of the horizontal axis should be noted. For example, the estimate at 2020 implies the annual accumulation

285   between 2020 and 2021. As summarized in Table 2, the depth of the deepest layer D_{max} observed at the crossover in Fig. 5(a)

and (b) is 70.78m for the 2018 dataset and 80.78 m for the 2021 dataset, with depositional ages of ~15 and ~18 years,

respectively. The deepest layer observed at the 2004 ice core and 2005 temperature sensor tower site is at 78.91 m with the

depositional age of ~18.6 years. The effective snow permittivity ε_{r_eff} in Table 2 is calculated as the ratio of D_{max} to the travel

time from the surface to the deepest layer observed by the radar. At the crossover, the estimated accumulation rate between

290   2005 and 2006 is 2.97 m w.e.a[-1]; the estimated average accumulation rate for the years between 2002 and 2021 is ~3.10 m

w.e.a^{-1}; the estimated average accumulation rate for the years between 1992 and 2004 is ~2.82 m w.e.a^{-1}, which was obtained by extrapolation based on the linear trend of an annual increase of ~0.022 m w.e.a^{-1}. At the ice core/tower site, the estimated accumulation rate between 2005 and 2006 is 2.82 m w.e.a^{-1}; the estimated average accumulation rate for the years between 2002 and 2021 is ~2.89 m w.e.a^{-1}; the estimated average accumulation rate for the years between 1992 and 2004 is ~2.74 m

295   w.e.a^{-1}, which was obtained by extrapolation based on the linear trend of an annual increase of ~0.011 m w.e.a^{-1}. We see the estimates of 2.82 m w.e.a^{-1} and 2.74 m w.e.a^{-1} at the ice core/tower site are very close to the ground-truth values of 2.75 m w.e.a^{-1} and 2.66 m w.e.a^{-1} (highlighted in red in Table 2) which were estimated from the actual accumulation measurements made between June 3, 2005 to December 8, 2005 with an extrapolation to June 22, 2006, and determined from the 2004 ice core using the dating of a tephra layer from the 1992 Mount Spur eruption, respectively [Kanamori et al., 2008].

300   **3.3 Observations along glaciers**

Distinct zones or glacier facies exist for ice sheets and glaciers. These facies are related to snow accumulation and ablation, and include dry snow facies, percolation facies, wet-snow facies and ice facies in order from high to low elevations [Benson, 1996]. Large scale monitoring of glacial facies provide useful information for hydrological planning (particularly in areas where glacier-fed melt is a significant contributor to total runoff) and potentially early detection of climate changes. Multi-

305   temporal ERS-1 satellite SAR data of 1992-1993 revealed the dry-snow facies, combined percolation and wet-snow facies, ice facies, transient melt areas and moraine [Partington, 1998]. In Partington's study over the area between the north-east slopes of Mount Wrangell and Nabesna Glacier, the elevation of the snowline was around 2100 m, the dry snowline was at elevations around 3460 m, and the combined percolation and wet snow facies were within elevations between 2100 m and 3460 m. We also flew over this same area during our 2018 and 2021 surveys, and observed the strata in dry snow facies, the combined

310   percolation and wet snow facies, and ice facies. Having presented sample radar echograms for the dry snow facies in section 3.2, here we present a sample radar echogram in Fig. 9(a) for the combined percolation and wet snow facies. Figure 9(b) is a plot of the flight line (in red) on the map to show the geolocations of the data, collected on May 25, 2018. The details of the strata are not very clear in this radar image because it is greatly compressed (over a long distance of ~30 km), resulting in low pixel resolutions. Therefore, we also present an image of higher pixel resolutions in Fig. 9(c) for the portion enclosed by the

315   two vertical blue lines in Fig. 9(a) to enhance the granularity of features in the observed strata. We notice that in both images there are some discontinuous layers between the surface and previous summer layer. These internal reflections are roughly parallel with the surface, and the intensity is higher at lower elevations. The melting and refreezing, which are occasional in the percolation and snow wet facies, might result in these reflections. The snow depth of the previous summer surface shows a high correlation with the glacier surface elevation which decreases from 2815 m to 1943 m as shown in Fig. 9(d), i.e. the

320   annual snow depth increases with elevation.

The boundaries between different glacier facies can be identified according to the stratigraphic features of subsurface layers and C-band radar backscattering signatures [Partington, 1998; Langley et al., 2008; Ramage et al., 2000]. There are many cases

in our airborne radar observations the snowline between the ice facies and wet-snow facies can be clearly identified. Figure 10
325 presents such an example for Kaskawulsh Glacier where the data was collected on May 10, 2021 over a distance of 15km
along the glacier's central line. The glacier's surface profile in the image is flattened to better show the snow layers in Fig.
10(a), and the WGS84 surface elevations of the glacier are between 1913.43 m and 2362.18 m as shown in Fig. 10(c). The
snowline location at 6.973 km is marked by the red vertical line in the radar echogram according to the following features
observed: 1) the previous summer surface (PSS) is distinct because of its high coherent reflections at most elevations; 2)
330 multiple snow layers are visible at elevations higher than the elevation of the snowline, and these layers converge towards the
snowline; 3) at elevations lower than the elevation of the snowline, the PSS is the only visible layer beneath the surface and
the backscattering is lower due to the lack of internal scattering sources. In the zone of ice facies, the PSS is the major source
of backscattering, while in the zone of wet-snow facies, the backscatter sources include multi-year accumulation layers and
volume scattering. The blue line in Fig. 10(b) gives the column-wise-averaged power in the rectangular box at the bottom of
335 Fig. 10(a), and the two horizontal blue dashed lines in this figure at -1.76 dB and 4.81 dB, present the total averaged
backscattering powers of the ice facies and wet-snow facies in the boxed region. The orange line in Fig. 10(b) gives the roll
angles to show that the power peak in the ice facies was caused by off-nadir backscattering when the aircraft rolled about 11.7°
to the right. The latitude and longitude of the snowline location are respectively 60.6970° and 139.3633°, and the surface
elevation of the snowline is 2105.55 m, as marked by the red circle in Fig. 10(c).

340

Table 3 summarizes the snowline locations and elevations identified from the 2019 data for Kaskawulsh, Steller, Logan,
Nabesna glaciers and the east Bagley Ice Field. The last column of the table lists the CReSIS data frames that show the
transition from the wet-snow facies to the ice facies. The supplementary section S4 gives the corresponding echograms.

4 Summary and conclusions

345 The major efforts and contribution from the studies presented in this paper include:

1) Successful collection of snow data using CReSIS S/C band compact radar during two field campaigns in Alaska in
2018 and 2021, respectively; the completion of the data processing, and identification of the seasonal snow
accumulation layer. The seasonal snow depths of the majority of the radar observations were between 3.2 m and 4.2
m in the 2018 dataset, and around 3 m in the 2021 dataset.

350 2) Observation of snow strata in ice facies, wet-snow/percolation facies and dry snow facies, and identification of the
wet-snow to ablation transition areas of several glaciers based on the features of snow strata and radar backscattering
characteristics.

3) Development of a method to estimate the average snow accumulation rate at the caldera of Mount Wrangell. This
method uses the radar observations of multi-year strata to constrain the uncertain parameters of interpretation models
355 based on the assumption that most of the snow layers at the caldera observed by the radar are annual accumulation

layers. The estimated snow accumulation rates are very close to the ground truth obtained at the 2004 ice core and 2005 temperature sensor tower site. The results verified the method, its assumption and the interpretation models. Future work may expand these results to the whole caldera for the snow accumulation spatial pattern using the gridded strata observations.

360   4) Release of the S/C band snow data we collected in the two campaigns in Alaska as part of NASA Operation IceBridge Mission. These datasets are valuable for hydrology, glaciology and radar backscattering studies.

Data availability. The radar data products are available at https://data.cresis.ku.edu/data/snow/2018_Alaska_SO/ and https://data.cresis.ku.edu/data/snow/2021_Alaska_SO/; they are also available at NSIDC at https://nsidc.org/data/IRSNO1B/.
365   The traced seasonal snow thickness data is available at https://data.cresis.ku.edu/data/misc/Alaska_seasonal_snow/ (last access: 26 May 2021).

Author contributions. All authors contributed to this work. JL participated in the campaigns, collected and processed the radar data, performed the analysis, and led the writing of the manuscript. FRM contributed to the radar system design and implementation, participated in the campaigns, and collected the radar data. CL contributed to the radar system design and the project management. JP contributed to the processing toolbox for the radar data. DGG contributed to the radar system design. EA contributed to the design and integration of the antenna for the radar system and participated in the 2018 campaign for antenna installation.

375   *Competing interests.* The authors declare that they have no conflict of interest.

References

385   Arcone, S. A.: Airborne-radar stratigraphy and electrical structure of temperate firn: Bagley Ice Field, Alaska, U.S.A., J. Glaciol., 48, 317 –334, 2002.

Benson, C. S.: Glaciological studies on Mount Wrangell, Alaska, 1961, Arctic, 21(3), 127–152, 1968.

Benson, C.S.: Ice core drilling on Mt. Wrangell, Alaska, 1982, CRREL Spec. Rep. 84-34, 61–68, 1984.

Benson, C. S: Stratigraphic studies in the snow and firn of the Greenland ice sheet, SIPRE Res. Rep. 70 [Revised edition of
390   1962 report], 1996.

Benson, C. S., Bingham, D. K., and Wharton, G. B.: Glaciological and volcanological studies at the summit of Mt. Wrangell,
Alaska, Int. Assoc. Sci. Hydrol. Pubk, 104, 95-98, 1975.

Benson, C. S., and Motyka, R. J.: Glacier-volcano interactions on Mt. Wrangell, Alaska, Annual Report, 1977-78, 1-25,
Geophys. Inst., Univ. of Alaska, Fairbanks, 1978.

395   Benson, C.S., Motyka, R.J., McNutt, S., Lüthi, M., and Truffer, M.: Glacial–volcano interactions in the North Crater of Mt.
Wrangell, Alaska, Ann. Glaciol., 45, 48–57, 2007.

Beaumont, R. T.: Mt. Hood pressure pillow snow gage, Journal of Applied Meteorology 4(5), 626–631, 1965.

Bingham, D. K.: Ice motion and heat flow studies on Mt. Wrangell, Alaska, M.S. thesis, Univ. of Alaska, Fairbanks, 1967.

Garry, K. C. C., and Guy, M. C.: Radar imaging of glaciovolcanic stratigraphy, Mount Wrangell caldera, Alaska: interpretation
400   model and results, Journal of Geophysical Research, 94(B6), 7237-7249, 1989.

Gusmeroli, A., Wolken, G. J., and Arendt, A. A.: Helicopter-borne radar imaging of snow cover on and around glaciers in
Alaska, Annals of Glaciology, 55(67), 78-88, 2014.

Kanamori, S., Okura, Y., and Yoshikawa, K.: Snow pit studies and radio-echo soundings on Mt. McKinley 2004, Bulletin of
Glaciological Research, 22, 89-97, 2005.

405   Kanamori, S., Benson, C. S., Truffer, M., Matoba, S.: Seasonality of snow accumulation at Mount Wrangell, Alaska, USA, J.
Glaciology, 54(185), 2008.

Lindsay, C., Zhu, J., Miller, A. E., Kirchner, P., and Wilson, T. L.: Deriving snow cover metrics for Alaska from
MODIS, Remote Sens., 2015, *7*, 12961-12985, 2015.

McGrath, D., Sass, L., O'Neel, S., Arendt, A., Wolken, G., Gusmeroli, A., Kienholz, C., and McNeil, C.: End-of-winter snow
410   depth variability on glaciers in Alaska, J. Geophys. Res. Earth Surf., 120, 1530–1550, 2015.

Hill, D. F., Bruhis, N., Calos, S. E., Arendt, A., and Beamer J.: Spatial and temporal variability of freshwater discharge into
the Gulf of Alaska, J. Geophys. Res. Oceans, 120, 634–646, 2015.

Langley, K., Hamran, S. E., Høgda, K. A., Storvold, R., Brandt, O., Kohler, J., and Hagen., J. O.: From glacier facies to SAR
backscatter zones via GPR, IEEE TGRS, 46(9), 2506-2516, 2008.

415   Largeron, C., Dumont, M., Morin, S., Boone, A., Lafaysse, M., Metref, S., Cosme, E., Jonas, T., Winstral, A., and Margulis
S. A.: Toward snow cover estimation in mountainous areas using modern data assimilation methods: a review, Front. Earth
Sci. 8(325), 1-21, 2020.

Li, J., Rodriguez-Morales, F., Arnold, E., Leuschen, C., Paden, J., Shang, J., Gomez-Garcia, D., and Larsen, C.: Airborne snow
measurements over Alaska mountains and glaciers with a compact FMCW radar, Proc. IEEE Int. Geosci. Remote Sens. Symp.,
420   Yokohama, Japan, 3966–3969, 2019.

Looyenga, H.: Dielectric constants of homogeneous mixture, Molecular Physics, 9(6), 501-511, 1965.

Motyka, R. J.: Increases and fluctuations in thermal activity at Mount Wrangell, Alaska, Ph.D. thesis, Univ. of Alaska, Fairbanks, 1983.

Matoba, S., Shimbori, K., and Shiraiwa, T.: Alpine ice-core drilling in the North Pacific region, Annals of Glaciology, 55(68), 2014.

Neal, E. G., Hood, E., and K. Smikrud, K.: Contribution of glacier run-off to freshwater discharge into the Gulf of Alaska, Geophys. Res. Lett., 37(6), L06404, 1-5, 2010.

Panzer, B., Gomez-Garcia, D., Leuschen, C., Paden, J., Rodriguez-Morales, F., Patel, A., Markus, T., Holt, B., and Gogineni, S.: An ultra-wideband, microwave radar for measuring snow thickness on sea ice and mapping near-surface internal layers in polar firn, J. Glaciology, 59(214), 244–254, 2013.

Partington, K.: Discrimination of glacier facies using multi-temporal SAR data, J. Glaciology, 44(146), 42-53, 1998.

Porter, S. E., Mosley-Thompson, E., and Thompson, L. G.: Ice core $\delta18O$ record linked to Western Arctic sea ice variability, JGR Atmospheres, 124(10), 10784-10801, 2019.

Ramage, J. M., Isacks, B. L., and Miller, M. M.: Radar glacier zones in southeast Alaska, U.S.A.: field and satellite observations, J. Glaciology, 46(153), 287-296, 2000.

Rodríguez-Morales, F., Li, J., Gomez-García, D., Shang, J., Arnold, E., Leuschen, C., Larsen, C. F., Shepherd, A., Hvidegaard, S. M., and Forsber, R.: A compact, reconfigurable, multi-UWB radar for snow thickness evaluation and altimetry: development and field trials, IEEE JSTARS, 14, 6755-6765, 2021.

Rodriguez-Morales, F., Occhiogrosso, V., and Arnold, E.: Multichannel UWB microwave radar front-end for fine-resolution measurements of terrestrial snow cover, Proc. 2021 Int. Conf. Radar Ant. Microw Electron. Telecomm., 120-124, 2021.

Hugonnet, R., McNabb, R., Berthier, E., Menounos, B., Nuth, C., Girod, L., Farinotti, D., Huss, M., Dussaillant, I., Brun, F., and Kääb, A.: Accelerated global glacier mass loss in the early twenty-first century, Nature, 592, 726–731, 2021.

Shanley, C. S., and Albert, D. M.: Climate change sensitivity index for pacific salmon habitat in Southeast Alaska, PLoS ONE 9(8): e104799, 1-13, 2014.

Stuefer, S. L., Kane, D. L., and Dean, K. M.: Snow water equivalent measurements in remote Arctic Alaska watersheds, Water Resources Research, 56(4), e2019WR025621, 1-12, 2020.

TIuri, M., Sihvola, A., Nyfors, E., and Hallikaiken, M.: The complex dielectric constant of snow at microwave frequencies, IEEE Journal of Oceanic Engineering, 9(5), 377-382, 1984.

Urmann, D.: Decadal scale climate variability during the last millennium as recorded by the Bona Churchill and Quelccaya Ice Cores, Dissertation, Ohio State University, 2009.

WCRP Global Sea Level Budget Group.: Global sea-level budget 1993–present, Earth Syst. Sci. Data 10, 1551–1590, 2018.

Winstral, A., Elder, K., and Davis, R.E.: Spatial snow modeling of wind-redistributed snow using terrain-based parameters, J. Hydrometeorology, 3, 524–538, 2002.

Yasunari, T. J., Shiraiwa, T., Kanamori, S., Fujii, Y., Igarashi, M., Yamazaki, K., Benson, C. S., and Hondoh, T.: Intra-annual

455   variations in atmospheric dust and tritium in the North Pacific region detected from an ice core from Mount Wrangell, Alaska.

J. Geophys. Res., 112, D10208, 2007.

Yan, J. B., Gogineni, S., Rodriguez-Morales, F., Gomez-Garcia, D., Paden J., Li, J., Leuschen, C. J., Braaten, D., Richter-

Menge, J., Farrell, S. L., Brozena, J., and Hale, R.: Airborne measurements of snow thickness: using ultrawide-band frequency-

modulated-continuous-wave radars, IEEE Geoscience and Remote Sensing Magazine, 5(2), 57-76, 2017.

460
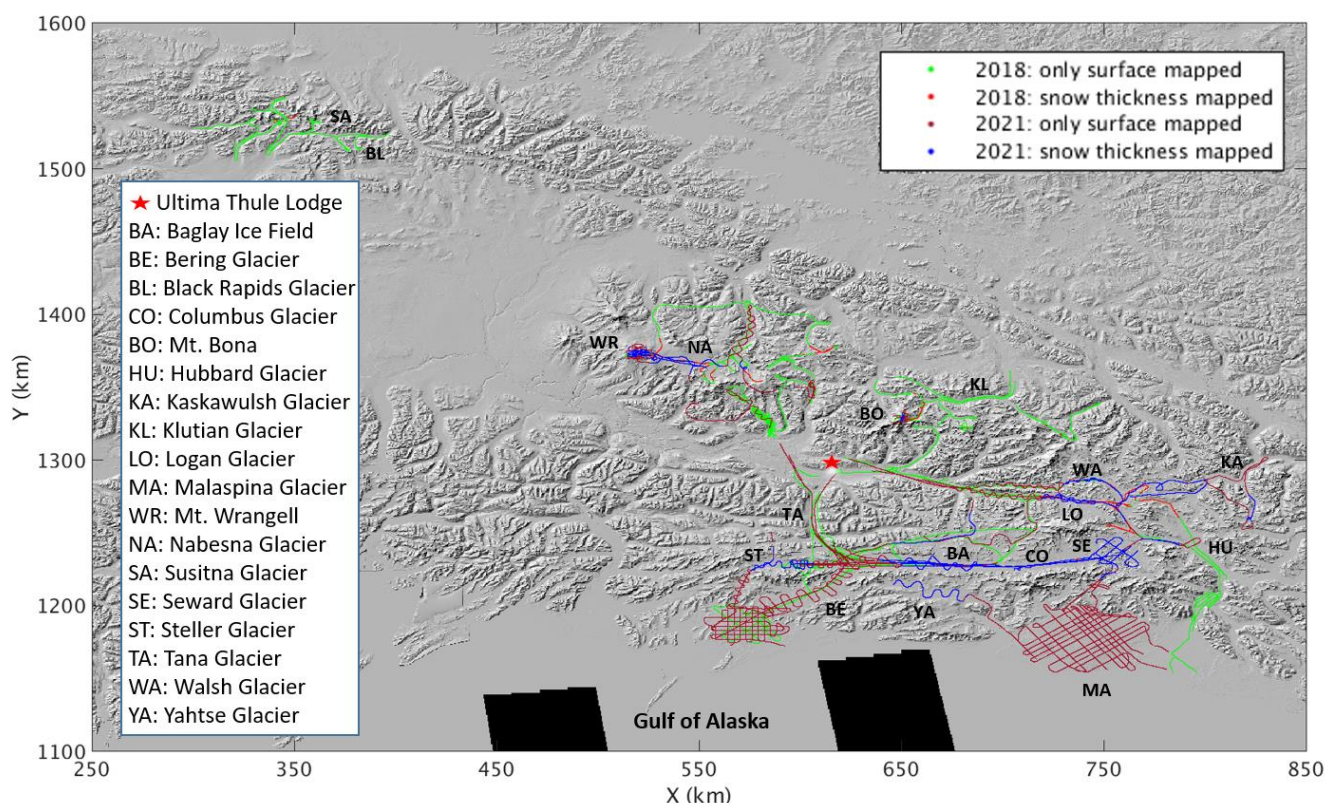
Figure 1: Coverage map of Snow Radar data from the OIB surveys in Alaska: flight lines in green and red colors represent the locations where the Snow Radar collected data in 2018; flight lines in brown and blue colors represent the locations where the Snow
465   **Radar collected data in 2021; and specifically the red and blue lines represent the locations where snow layer or snow-ice interface or snow-rock interface below the surface were observed by the compact Snow Radar. The hillshade map in the background was provided by Dr. C. Larsen.**
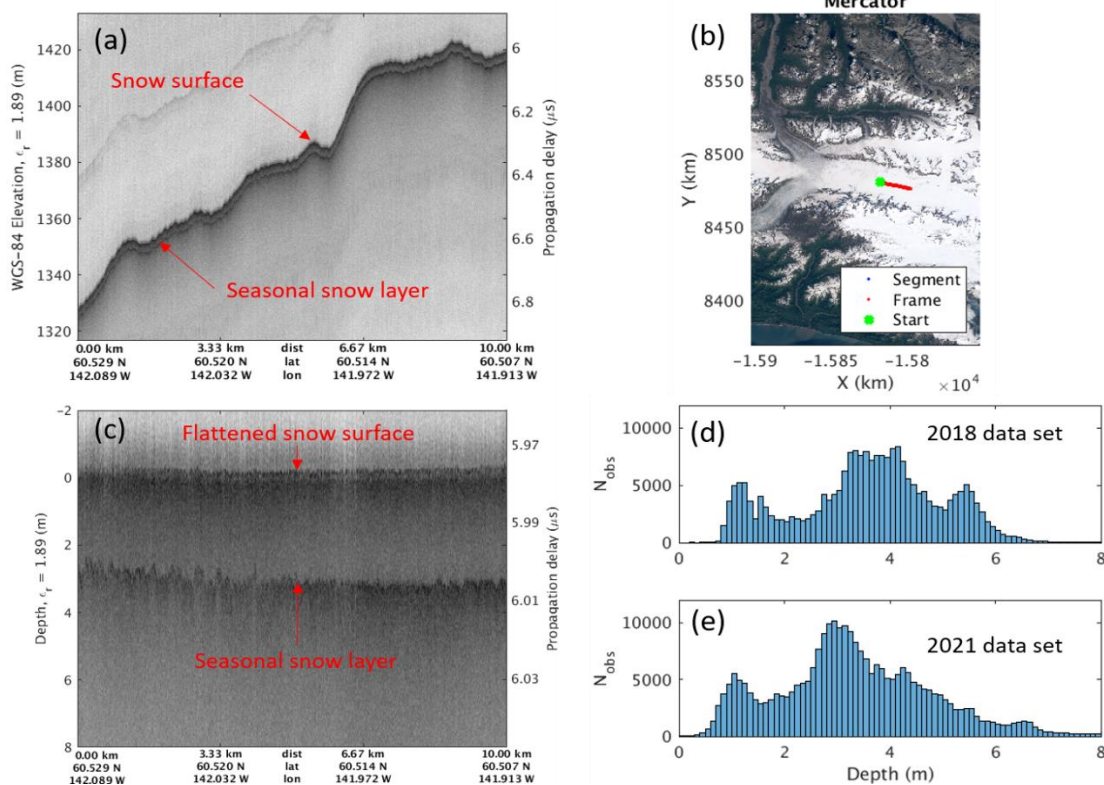
Figure 2: (a) Seasonal snow observations in Bagley Ice Field; (b) Geolocations of the radar echogram indicated by the red line on
470 **the Landsat image map; (c) Snow depth around 3 m shown after the glacier surface profile is flattened; (d) and (e) Tracked seasonal**
snow depth distributions of 2018 and 2021 datasets.
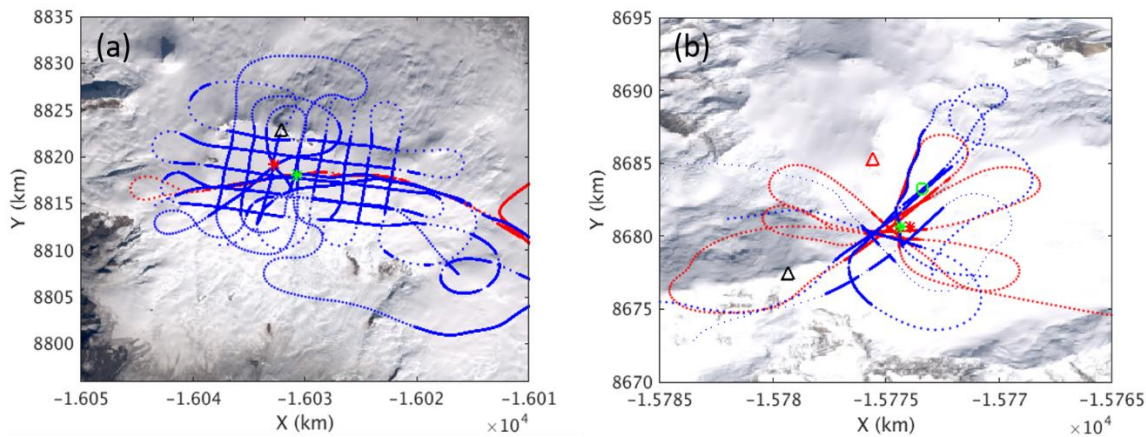
Figure 3: Data coverage over (a) Mount Wrangell and (b) Mount Bona summit areas plotted on the Landsat image maps. The dots
with visible spacing depict flight lines and the dots without visible spacing represent the locations with snow layer/ snow-ice
475 **interface/snow-rock interface observations. The red and blue dots represent the flight lines of 2018 and 2021 respectively.**
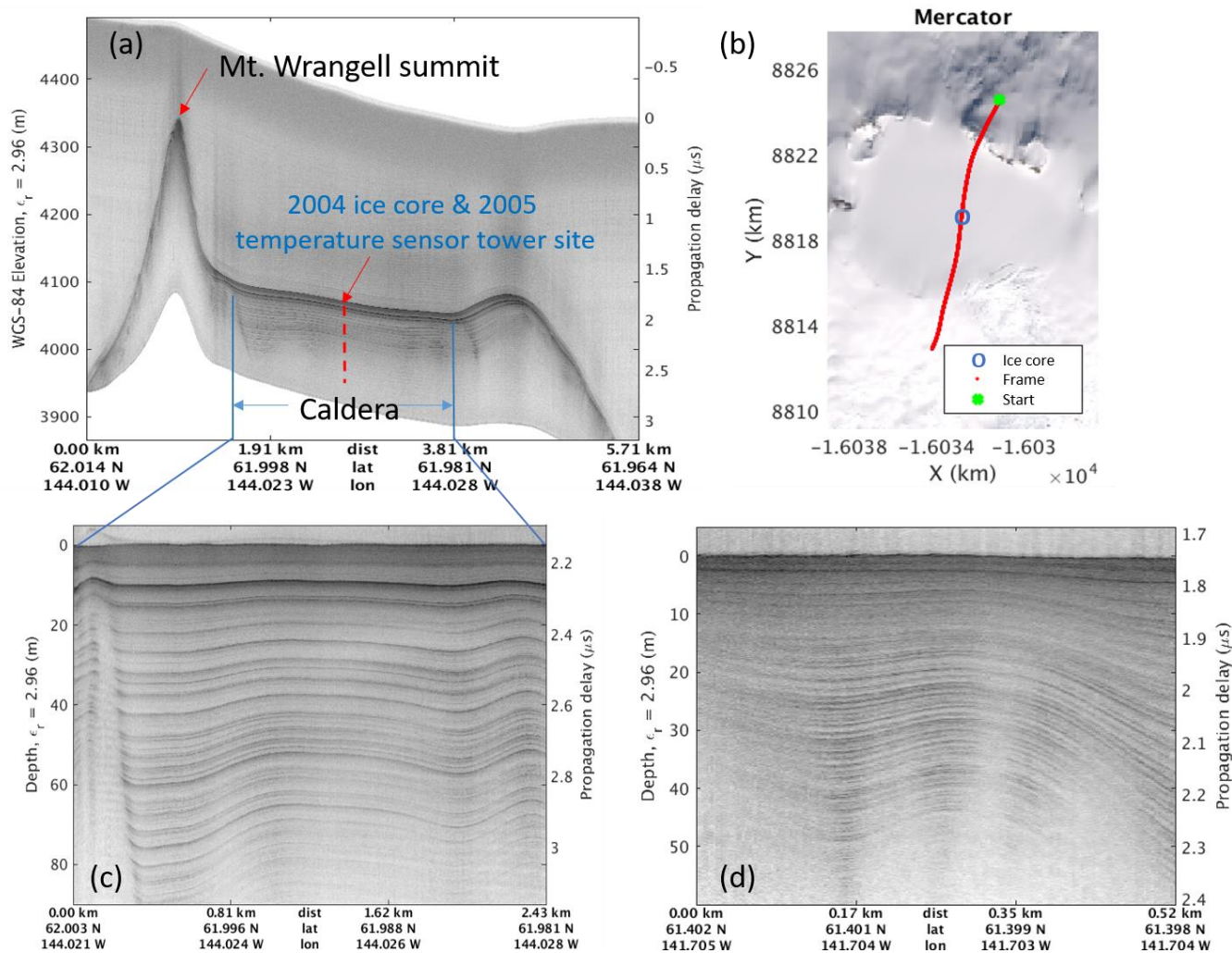
Figure 4: Conformable snow layers observed at mountain summit areas. (a) Mount Wrangell, data collected on May 9, 2021; (b) the flight line in red annotates the geolocations of the echogram in (a) on the Landsat image map; (c) Accumulation layers in the Caldera; and (d) Bona-Churchill, data collected on May 9, 2021; its location, marked by the green star in Fig. 3b, is close to the 2002 BC1 ice core drilling site. The snow surface profiles in (c) and (d) are both flattened for to better display the layers.
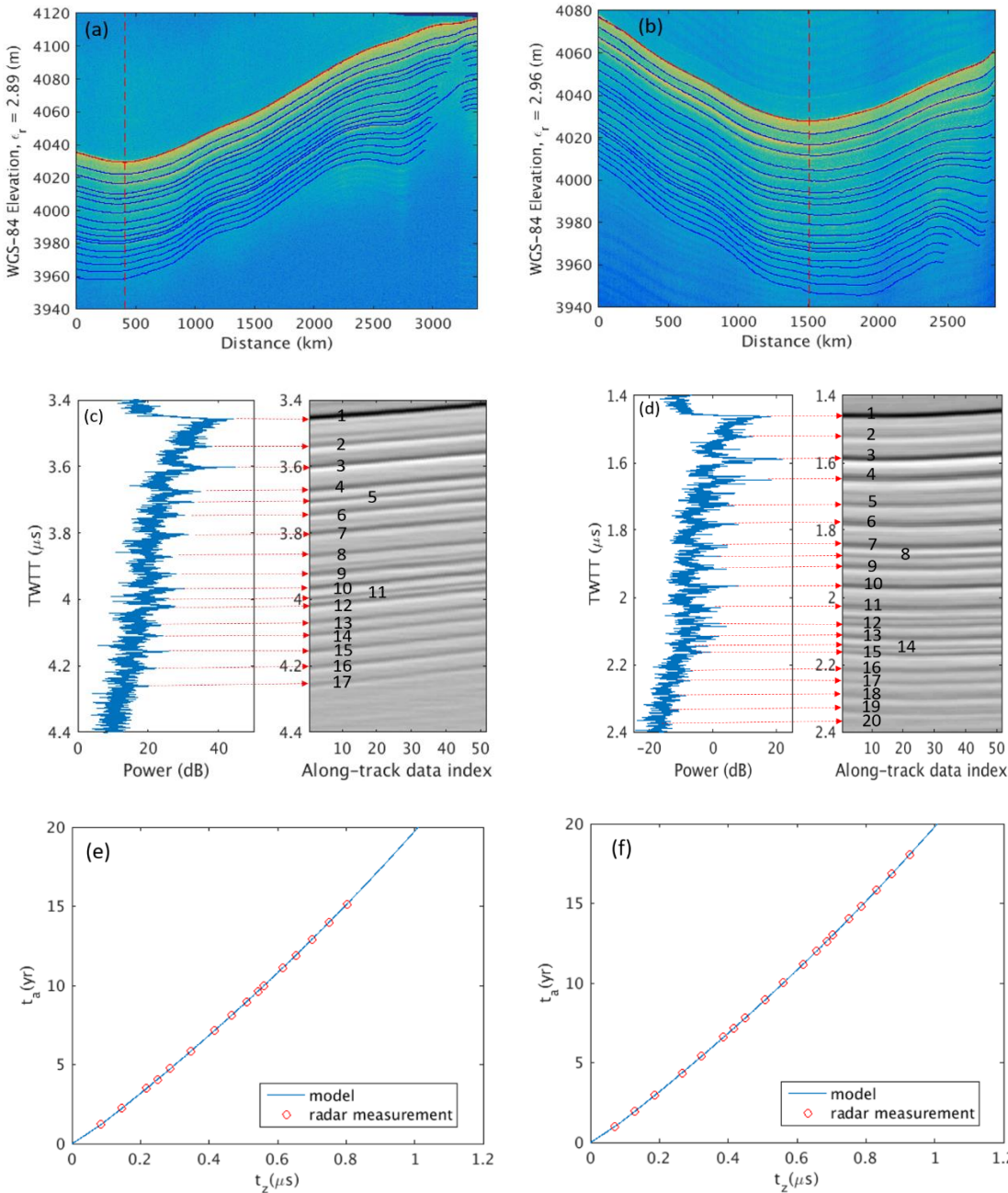
Figure 5: (a) Tracked snow layers using the 2018 dataset (plotted with ε_r = 2.89 based on the mean velocity between the surface and the depth of 70.80 m at the crossover marked by the vertical dashed red line); (b) Tracked snow layers using the 2021 dataset(plotted with ε_r = 2.96 based on the mean velocity between the surface and the depth of 80.78 m at the crossover marked by the vertical dashed red line); (c) On the left is the A-scope at the crossover in 2018; On the right are the picked layers marked by sequence numbers after along-track filtering; (d) On the left is the A-scope at the crossover in 2021; On the right are the picked layers marked
by sequence numbers after along-track filtering; (e) and (f) Snow layer ages based on model and radar measurements of the TWTTs between the surface and the tracked layers at the location of the vertical red dashed line, from 2018 and 2021 data frame, reflectively.

18
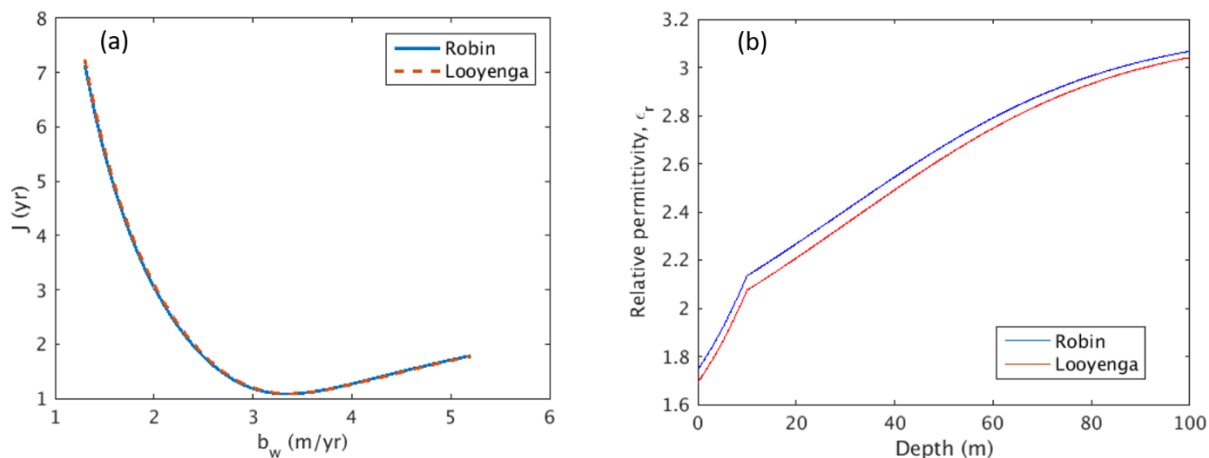
495 **Figure 6: (a) Cost function of layer ages versus water equivalent surface balance; (b) Empirical density-permittivity models**
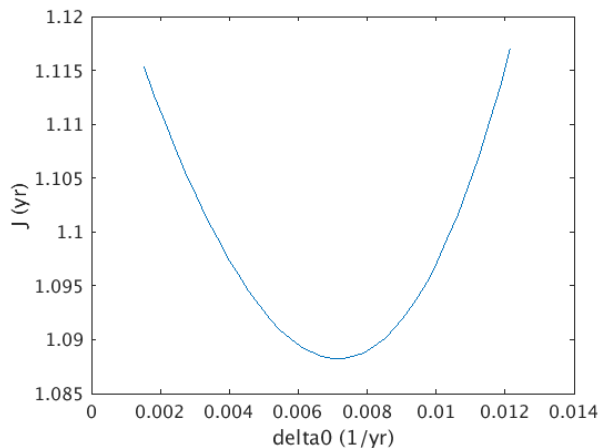

Figure 7: Cost function of layer ages versus Δ_0
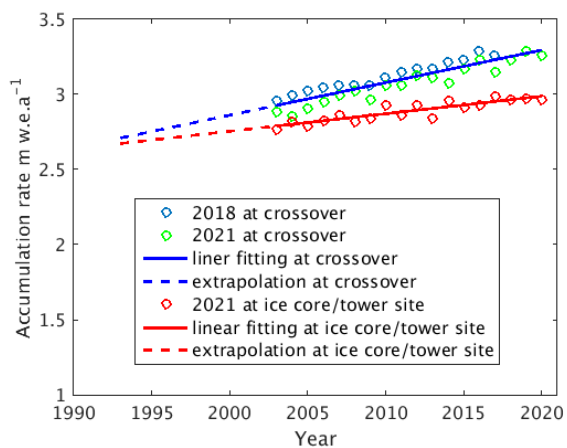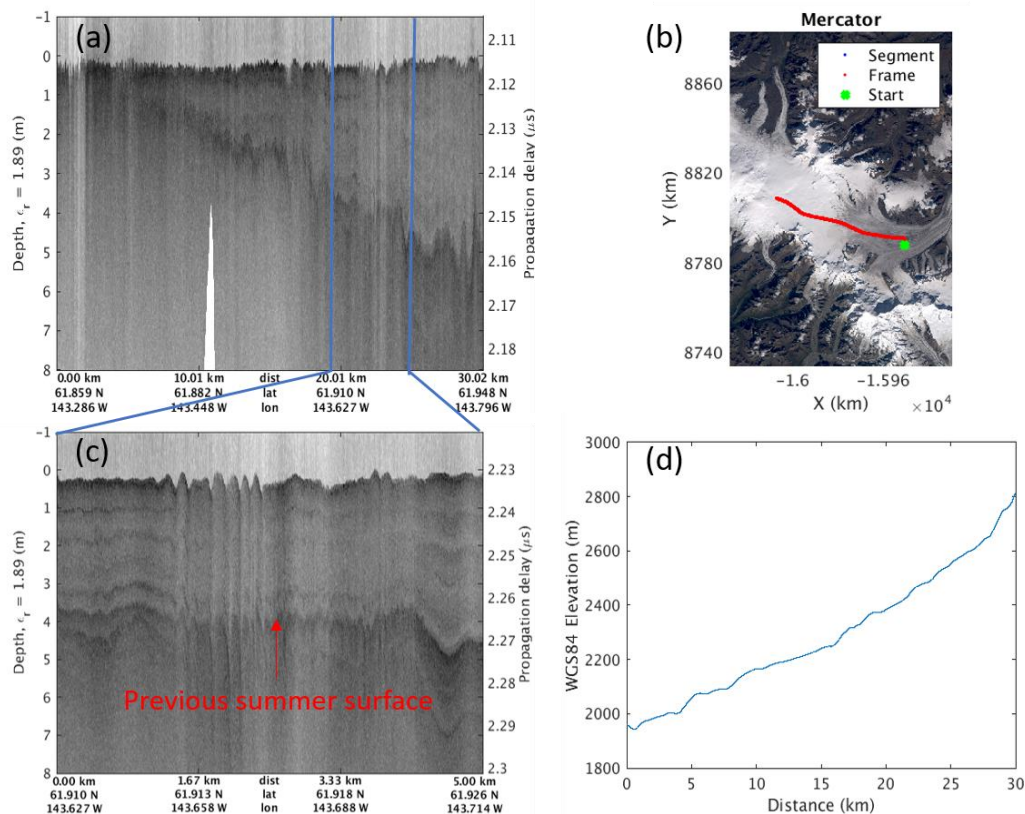
Figure 8: Estimated annual accumulation rates

500

Figure 9: (a) Observations from the east of Mount Wrangell to Nabesna Glacier; (b) The flight line plotted in red on the Landsat image map; (c) The radar echogram image with clear strata details for the portion between 20 km and 25 km in (a); (d) The surface elevation profile along the flight line.
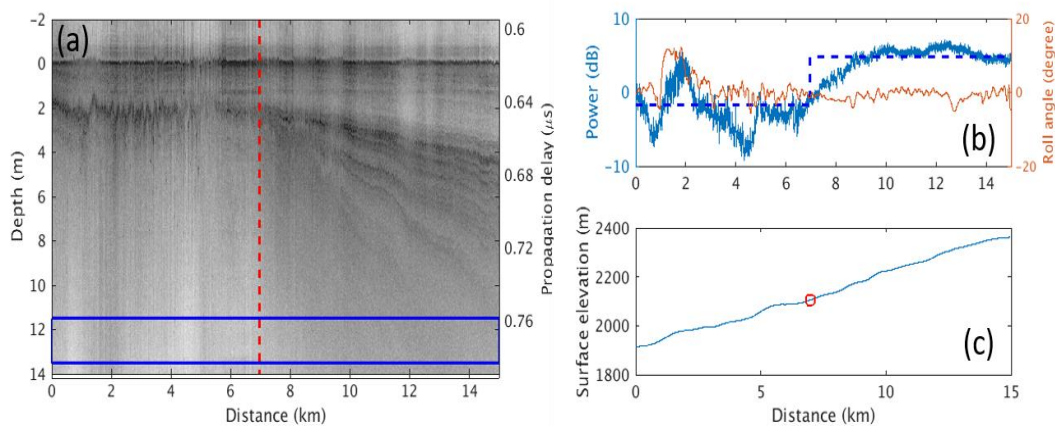

Figure 10: Snow stratigraphic features during the transition from wet-snow facies to ice facies

510 **Table 1: Estimated depositional ages of tracked layers**

Crossover of 2018 & 2021 datasets											
$(b_w = 3.3\ m/yr,\ \Delta_0 = 7.3/7.6 \times 10^{-3}\ /yr\ \&\ J = 1.11/1.08\ yr\ for\ 2018/2021)$											
2018	Layer index i	2	3	4	5	6	7	8	9	10	11	12
	t_a (yr)	1.19	2.20	3.43	4.00	4.67	5.77	7.06	8.04	8.88	9.52	9.87
	Layer index i	13	14	15	16	17						
	t_a (yr)	10.99	11.78	12.78	13.86	15.03						
2021	Layer index i	2	3	4	5	6	7	8	9	10	11	12
	t_a (yr)	0.98	1.92	2.9	4.29	5.32	6.51	7.09	7.74	8.83	9.90	11.09
	Layer index i	13	14	15	16	17	18	19	20			
	t_a (yr)	11.89	12.52	12.89	13.93	14.68	15.70	16.73	17.96			
2004/ 2005 ice core & temperature sensor tower site											
$(b_w = 3.0\ m/yr,\ \Delta_0 = 3.9 \times 10^{-3}\ /yr\ \&\ J = 1.33\ yr)$											
2001	Layer index i	2	3	4	5	6	7	8	9	10	11	12
	t_a (yr)	0.85	1.67	2.64	3.92	4.86	5.88	6.43	7.04	8.00	9.08	10.13
	Layer index i	13	14	15	16	17	18	19	20	21	22	
	t_a (yr)	10.72	11.24	11.59	12.63	13.22	14.05	14.98	16.02	17.54	18.60	

* Refer to the layers marked by the numbers in Fig. 5 (c) and (d) for the layer index i.

Table 2: Maximum layer depth observed D_{max}, effective snow relative permittivity ε_{r_eff} and accumulation rates r_a estimated at the two study sites.

	2004/ 2005 ice core & temperature sensor tower site (61.9908°N, 144.0256°W)			2018/2021 crossover (61.9859° N, 144.0068°W)
D_{max} (m)	78.91			70.78/80.78
ε_{r_eff}	2.96			2.89/2.96
r_a (m w. e. a^{-1})	Radar	Temperature sensor	Ice core	Radar
2005-2006	2.82	2.75	NA	2.97
2002-2021 (averaged)	2.89	NA	NA	3.10
1992-2004 (averaged)	2.74	NA	2.66	2.82
Linear trend (m w. e. a^{-2})	0.011	NA	NA	0.022

515

Table 3: Snowline locations of glaciers and ice fields

Glacier name	Snowline location			CReSIS data frames (YYYYMMDD_SS_FFF-FFF)*
	Latitude (°N)	Longitude (°W)	Elevation	
Kaskawulsh	60.7501	139.3066	2062.00	20210510_03_001-006
	60.6970	139.3633	2105.55	20210510_03_039-041
Steller	60.5913	143.4026	1325.90	20210512_02_003-005
Logan	60.7215	140.1521	2161.84	20210513_02_045-046
Nabesna	61.8658	143.4937	2176.01^{+1}	20210503_02_015-018
E. Bagley	60.4967	141.7715	1528.14^{+2}	20210513_02_002-006

* In the data frame names, Y, M, D, S, F represent year, month, day, data segment, and data frames, respectively.
$^{+1}$ Compared to 2100 m in [Partington, 1998]. $^{+2}$ Compared to ~1320 m [Arcone, 1998].

520